

# Combined Spin- and Gradient-Echo Perfusion-Weighted Imaging

Heiko Schmiedeskamp,<sup>1</sup> Matus Straka,<sup>1</sup> Rexford D. Newbould,<sup>2</sup> Greg Zaharchuk,<sup>1</sup> Jalal B. Andre,<sup>1</sup> Jean-Marc Olivot,<sup>3</sup> Michael E. Moseley,<sup>1</sup> Gregory W. Albers,<sup>3</sup> and Roland Bammer<sup>1\*</sup>

**In this study, a spin- and gradient-echo echo-planar imaging (SAGE EPI) MRI pulse sequence is presented that allows simultaneous measurements of gradient-echo and spin-echo dynamic susceptibility-contrast perfusion-weighted imaging data. Following signal excitation, five readout trains were acquired using spin- and gradient-echo echo-planar imaging, all of them with echo times of less than 100 ms. Contrast agent concentrations in brain tissue were determined based on absolute  $R_2^*$  and  $R_2$  estimates rather than relative changes in the signals of individual echo trains, producing  $T_1$ -independent dynamic susceptibility-contrast perfusion-weighted imaging data. Moreover, this acquisition technique enabled vessel size imaging through the simultaneous quantification of  $R_2^*$  and  $R_2$ , without an increase in acquisition time. In this work, the concepts of SAGE EPI pulse sequence and results in stroke and tumor imaging are presented. Overall, SAGE EPI combined the advantages of higher sensitivity to contrast agent passage of gradient-echo perfusion-weighted imaging with better microvascular selectivity of spin-echo perfusion-weighted imaging. Magn Reson Med 68:30–40, 2012. ©2011 Wiley Periodicals, Inc.**

**Key words:** spin-echo EPI; gradient-echo EPI; multiecho acquisition; dynamic susceptibility-weighted perfusion-weighted imaging; SAGE PWI

Dynamic susceptibility-contrast perfusion-weighted imaging (DSC-PWI) is a well-established MRI acquisition technique to measure hemodynamic properties in vivo following a gadolinium (Gd)-based contrast agent bolus injection (1–4). DSC-PWI can reveal important abnormal vascular information in stroke patients by measuring cerebral blood flow (CBF), cerebral blood volume (CBV), mean transit time (MTT), and time-to-maximum of the residue function ( $T_{max}$ ) (5–8). These parameters provide valuable information for triaging stroke patients to more advanced therapies (9,10). In

tumor patients, CBV, CBF, and the mean vessel size distribution, facilitated by vessel size imaging (VSI), reveal important hemodynamic and underlying microvascular information to monitor tumor growth and treatment (11–15).

Because of its relatively high contrast-to-noise ratio, gradient-echo DSC-PWI (GE-PWI) is the method of choice for routine clinical applications of DSC-PWI. GE-PWI is equally sensitive to a broad range of (macro)vessel diameters, with reduced sensitivity to the microvascular range. In contrast, despite its lower overall sensitivity to contrast agent-induced signal variations, spin-echo DSC-PWI (SE-PWI) exhibits a peak sensitivity to the microvasculature, including arterioles, capillaries, and venules. These differences in sensitivity to the vascular properties were shown in simulations studies (16,17) and verified in practice (18).

In clinical MRI exams, measurements of both GE-PWI and SE-PWI may increase the diagnostic value of DSC-PWI acquisitions, justified by differences in sensitivity within each voxel to the size of the vasculature. After reperfusion therapy, for example, ischemic tissue may appear salvaged on GE-PWI maps due to reperfusion on the macrovascular level. However, CBF extracted from SE-PWI data might still be reduced, indicating the failure of microvascular reperfusion and thus the loss of proper tissue function. This tissue state is often referred to as the “focal no-reflow” phenomenon (cf. Refs. 19 and 20), which cannot be properly diagnosed with standard GE-PWI methods alone. Therefore, simultaneous measurements of GE-PWI and SE-PWI may reveal complementary information in clinical MRI exams.

The development of a combined gradient-echo (GE) and spin-echo (SE) echo-planar imaging (EPI) pulse sequence (21) facilitated the simultaneous acquisition of GE and SE perfusion data (13), and it enabled the determination of VSI maps, which are based on the combination of GE and SE data (15,22). With this combined approach, GE-PWI, SE-PWI, and VSI are obtained from the same DSC-PWI acquisition, without adding additional scan time or a second bolus injection.

However, the MRI pulses sequences used in (13,15,21,22) have the drawback that they are all sensitive to  $T_1$ -shortening effects caused by the passage of a Gd tracer through the bloodstream. Generally, DSC-PWI relies on  $T_2^*$ - or  $T_2$ -shortening effects that cause MRI signal attenuation during contrast agent passage. However,  $T_1$ -shortening effects of Gd-based contrast agents in time-resolved DSC-PWI acquisitions counter this signal

<sup>1</sup>Lucas Center, Department of Radiology, Stanford University, Stanford, California, USA.

<sup>2</sup>GSK Clinical Imaging Centre, Hammersmith Hospital, London, United Kingdom.

<sup>3</sup>Stanford Stroke Center, Department of Neurology and Neurological Sciences, Stanford University Medical Center, Stanford, California, USA.

Grant sponsor: National Institute of Health; Grant numbers: R01EB002711, R01NS047607, R01NS034866, R01NS066506, P41RR009784; Grant sponsors: Lucas Foundation, Oak Foundation.

\*Correspondence to: Roland Bammer, Ph.D., Associate Professor of Radiology, Lucas Center, Department of Radiology, Stanford University, 1201 Welch Road, Stanford, CA 94305-5488. E-mail: rbammer@stanford.edu

Received 14 June 2011; revised 21 July 2011; accepted 2 August 2011.

DOI 10.1002/mrm.23195

Published online 23 November 2011 in Wiley Online Library (wileyonlinelibrary.com).

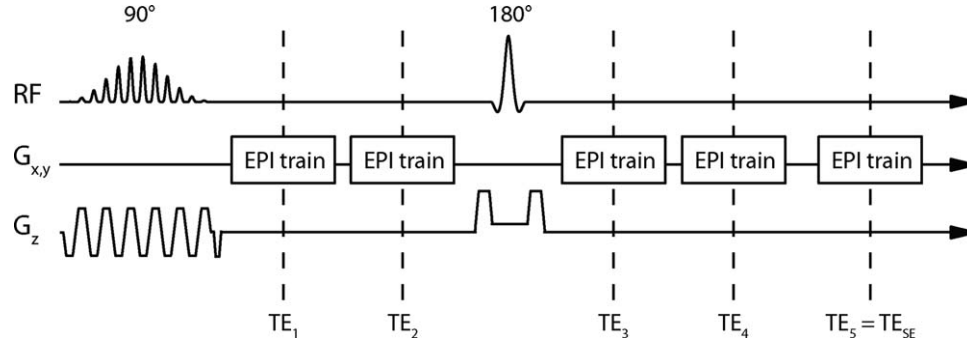


FIG. 1. Pulse sequence diagram of SAGE EPI pulse sequence: a spectral-spatial signal excitation pulse is followed by two EPI readout trains acquired at echo times  $TE_1$  and  $TE_2$ , a  $180^\circ$  refocusing pulse, and three more EPI readouts ( $TE_3$ – $TE_5$ ), with the last readout at  $TE_5 = TE_{SE}$  resulting in a SE signal.

attenuation (23,24). As a result, the measured MRI signal might increase after the bolus passage. This increase becomes more pronounced with increasing temporal resolution. In recently published guidelines by the Stroke Imaging Repository Consortium, a temporal resolution of 2 s or lower is suggested for DSC-PWI acquisitions (25), leading to considerable  $T_1$ -shortening effects. These  $T_1$  effects induce errors in the DSC-PWI quantification by altering the shapes of the arterial input function (AIF) and the tracer concentration curves in tissue (24). Several techniques have been suggested to mitigate or eliminate  $T_1$ -shortening effects, among them were correction algorithms (26), a predosage with a small amount of Gd-based contrast agent (27), MRI pulse sequences that use excitation pulses with lower flip angles, or multiecho GE-PWI methods in which tracer concentrations are based on absolute  $R_2^*(t)$  instead of its relative changes (28,29). Although all of these methods were able to counteract  $T_1$  effects to a certain degree, a recently published, comparative study in tumor patients showed that a dual-echo acquisition technique was one of the most robust methods in the determination of tumor CBV (30). These results particularly arise from the fact that  $T_1$  effects can severely confound perfusion parameters in the presence of a disrupted blood-brain barrier (BBB), i.e., if some of the contrast agent is leaking into the extravascular space.

This work, motivated by these findings, focuses on a combined multiecho GE and SE EPI acquisition for quantitative DSC-PWI. A recently presented method for simultaneous quantification of  $R_2^*(t)$  and  $R_2(t)$  (31) was extended to obtain quantitative,  $T_1$ -independent  $R_2^*$ - and  $R_2$ -based DSC-PWI. The acquisition of multiple EPI images between a  $90^\circ$  excitation pulse and a  $180^\circ$  refocusing pulse as well as between the refocusing pulse and SE formation at a given echo time (TE) was achieved through the incorporation of parallel imaging to shorten the EPI readout trains. Side-by-side comparisons of  $T_1$ -independent  $R_2^*$ - and  $R_2$ -based DSC-PWI maps with conventional GE-PWI and SE-PWI maps revealed differences in vascular sensitivity and presentation of pathologies. Image acquisitions with the presented pulse sequence and the use of corresponding postprocessing methods resulted in improvements in both stroke and tumor DSC-PWI, particularly in the

presence of a disrupted BBB. In addition, the determination of absolute  $R_2^*(t)$  and  $R_2(t)$  facilitated the calculation of relative VSI maps.

## MATERIALS AND METHODS

Our experiments were conducted in 40 patients undergoing clinical brain MRI scans with contrast agent injection. Informed consent was obtained from all patients in compliance with our institute's internal review board. The acquisition and postprocessing methods used in this study rely on off-label use of Gd-based contrast agents. To obtain quantitative DSC-PWI values, we used the acquisition and postprocessing steps highlighted in the following sections.

### Experimental Setup and Data Acquisition

DSC-PWI data were acquired using a spin- and gradient-echo (SAGE) EPI pulse sequence shown in Fig. 1. The SAGE EPI pulse sequence is similar to the multiecho PERMEATE (perfusion with multiple echoes and temporal enhancement) sequence described previously (29), extended by a  $180^\circ$  refocusing pulse and additional EPI readout trains to measure both GE and SE data (32). For the purposes of this study, a  $90^\circ$  spectral-spatial excitation pulse, which excites water-signal only, was followed by multiple EPI readout trains. The operator was able to set the desired TE of the SE EPI readout in the graphical user interface of the scanner. All additional EPI trains were automatically placed before and after the  $180^\circ$  refocusing pulse. Parallel imaging with a reduction factor of 3 was used to reduce the EPI readout duration and to increase the number of EPI readouts that could be placed between signal excitation and SE readout.

Image acquisition was performed on a 3 T MRI system (General Electric Healthcare, Waukesha, WI) with a maximum gradient strength of 50 mT/m and gradient slew rate of 200 T/m/s, using an eight-channel head receiver array (Invivo Corporation, Orlando, FL). A five-echo SAGE EPI acquisition was used with  $TE_{1-5} = 16.6, 34.1, 61.8, 79.2,$  and  $97.0$  ms and with an echo-train duration of 15.3 ms. The last echo train acquired at  $TE_5 = TE_{SE} = 97$  ms coincided with the SE formation. A total of 15 slices were scanned with an acquisition matrix of  $84 \times 84$

within a field-of-view of 24 cm. Slice thickness was 5.0 mm with a gap of 2.0 mm. A 90° spectral-spatial radio-frequency excitation pulse was followed by a 180° SE refocusing pulse. Both pulses were developed using the Shinnar-Le Roux design algorithm (33–38), with the goal of a matched pair of radiofrequency pulses to prevent signal changes between echo trains acquired before and after the refocusing pulse; such signal changes are caused by differences in excitation and refocusing slice volumes (31). DSC-PWI was based on the subsequent acquisition of 63 volumes with a repetition time of 1800 ms, resulting in a total acquisition time of 1:53 min. The image acquisition parameters used in this study are summarized in Table 1.

### Image Reconstruction

The first three out of 63 imaging volumes were discarded to assure that the signal had reached a steady state. The next three volumes were used for the determination of entropy-based (field-of-view/2) ghost correction and ramp sampling correction parameters (39) as well as for parallel imaging calibration using GRAPPA [generalized autocalibrating partially parallel acquisitions (40)] with a 2D kernel size of  $2 \cdot k_y \times 5 \cdot k_x$   $k$ -space points (41). The GRAPPA kernel as well as linear and constant ghost correction parameters were applied to the remaining 57 volumes, which comprised the actual data used for perfusion analysis. Hereby, only the first interleave was repeatedly acquired to prevent signal instabilities caused by echo-time shifting. More specific details about the EPI readout and parallel imaging calibration scheme used for this study can be found elsewhere (29). All data were processed on a coil-by-coil basis; magnitude images were obtained as absolute values of complex sum-of-squares averages of the individual coil images. All images were zero-filled in  $k$ -space to a final image resolution of  $128 \times 128$  voxels in each slice.

### Contrast Agent Injection

A single-dose bolus (0.1 mmol/kg body weight) of a Gd-based contrast agent [gadopentetate dimeglumine (Gd-DTPA) or gadobenate dimeglumine (Gd-BOPTA)] was administered intravenously with an MRI-compatible power injector (Medrad Incorporation, Warrendale, PA), using a flow rate of 4–5 mL/s and a typical injection delay of 15–18 s. The contrast agent bolus was immediately followed by a minimum of 20 mL of saline, injected at the same flow rate, to push the tracer material out of the intravenous injection line and into the patient's heart.

### Determination of Contrast Agent Concentrations

Perfusion maps were obtained using the RAPID (rapid processing of perfusion and diffusion) postprocessing software (42), which was adjusted such that the tracer concentration in tissue,  $c_t(t)$ , was derived from voxel-wise changes in  $R_2^*$  and  $R_2$ . Here,  $R_2^*$ - and  $R_2$ -based tracer concentrations were obtained from

$$c_{t,R_2^*}(t) = x_1 \cdot \Delta R_2^*(t) = x_1 \cdot (R_2^*(t) - R_{2, \text{baseline}}^*) \quad [1]$$

Table 1  
Acquisition Parameters Used in the SAGE EPI Sequence

Parallel imaging reduction factor	3
Number of echoes	5
Matrix size ( $k_x \times k_y$ )	84 × 84 (zero-filled to 128 × 128)
Number of slices	15
Repetition time	1800 ms
Echo times	TE <sub>1</sub> = 16.6 ms TE <sub>2</sub> = 34.1 ms TE <sub>3</sub> = 61.8 ms TE <sub>4</sub> = 79.2 ms TE <sub>5</sub> = 97.0 ms
Acquisition time of each EPI train	15.3 ms

and

$$c_{t,R_2}(t) = x_2 \cdot \Delta R_2(t) = x_2 \cdot (R_2(t) - R_{2, \text{baseline}}) \quad [2]$$

$c_{t,R_2^*}(t)$  and  $c_{t,R_2}(t)$  are the time-dependent  $R_2^*$ - and  $R_2$ -based tracer concentrations, and  $x_1$  and  $x_2$  are the scaling factors that relate changes in transversal relaxation times to absolute tracer concentrations. For this study, we used a scaling factor of  $x_1 = 11.5$  ms mmol, derived from Ref. 43.  $x_2$  was preliminarily determined from the median of the ratio of  $R_2$ -based CBF to  $R_2^*$ -based CBF values, computed across voxels within white matter, and averaged over all 40 patients (44). This analysis resulted in  $x_2 = 4.25 \cdot x_1 = 48.9$  ms mmol.

$R_2^*$  and  $R_2$  baseline estimates were calculated from pre-bolus signal averages using the following MRI signal equation:

$$S(\tau) = \begin{cases} S_0^I \cdot e^{-\tau \cdot R_2^*} & , 0 < \tau < TE_{SE}/2 \\ S_0^{II} \cdot e^{-TE_{SE} \cdot (R_2^* - R_2)} \cdot e^{-\tau \cdot (2 \cdot R_2 - R_2^*)} & , TE_{SE}/2 < \tau \leq TE_{SE} \end{cases} \quad [3]$$

where  $S(\tau)$  is the MRI signal acquired at the echo time  $\tau$  at one time point of a SAGE EPI time series. Voxel-wise estimates of  $S_0^I$ ,  $S_0^{II}$ ,  $R_2$ , and  $R_2^*$  were obtained through a least-squares solution of Eq. 3 from the average signal during the prebolus period. From these estimates, an additional parameter  $\delta = S_0^I/S_0^{II}$  was calculated, which accounts for residual signal differences—caused by imperfectly matched slice profiles—between echo trains acquired before and after the refocusing pulse (31). The voxel-wise estimates of  $\delta$  were assumed to remain constant for the whole duration of the DSC-PWI acquisition. Thus, the least-squares solution of Eq. 3 for each time point consisted of three instead of four unknowns, i.e.,  $S_0^I(t)$ ,  $R_2(t)$ , and  $R_2^*(t)$ . With the reduction to a three-parameter fit, we achieved better temporal signal stability compared to a four-parameter fit (data not shown).

The resulting DSC-PWI maps derived from Eqs. 1 and 2 and Ref. 42 were compared to GE-PWI maps obtained from data acquired at TE<sub>2</sub> = 34.1 ms and to SE-PWI maps obtained from data acquired at TE<sub>5</sub> = 97.0 ms. These datasets resembled standard single-echo GE-PWI and SE-PWI acquisitions, respectively. Tracer concentrations used for GE-PWI maps were obtained with

$$c_{t,GE}(t) = x_1 \cdot \Delta R_2^*(t) = x_1 \cdot \left( -\frac{1}{TE_2} \cdot \log\left(\frac{S_{GE}(t)}{S_{0,GE}}\right) \right), \quad [4]$$

and those used for SE-PWI maps with

$$c_{t,SE}(t) = x_2 \cdot \Delta R_2(t) = x_2 \cdot \left( -\frac{1}{TE_5} \cdot \log\left(\frac{S_{SE}(t)}{S_{0,SE}}\right) \right). \quad [5]$$

$S_{GE}(t)$  is the time-dependent magnitude signal of the second GE EPI train acquired at  $TE_2 = 34.1$  ms, and  $S_{0,GE}$  is its prebolus baseline signal average. Conversely,  $S_{SE}(t)$  is the voxel-wise temporal signal magnitude of the SE EPI train measured at  $TE_5 = 97$  ms, and  $S_{0,SE}$  is its prebolus baseline signal average. Note that  $x_1$  and  $x_2$  are the scaling factors already used for the determination of  $R_2^*$ - and  $R_2$ -based tracer concentrations.

### Vessel Size Imaging

For tumor imaging, relative VSI maps were extracted from the ratios of  $R_2^*$ - to  $R_2$ -based CBV values to obtain  $T_1$ -independent data (45). Relative VSI maps were determined according to

$$VSI_{relative} = \frac{\int c_{t,R_2^*}(t) dt}{\int c_{t,R_2}(t) dt} \propto \frac{\int \Delta R_2^*(t) dt}{\int \Delta R_2(t) dt}, \quad [6]$$

with the numerical integration performed using the trapezoid rule.

### AIF Determination

The AIF needed for CBF quantification (46,47) was obtained from multiecho,  $R_2^*$ -based tracer concentrations within the internal carotid artery or the middle cerebral artery. Hereby, a quadratic model that relates changes in  $R_2^*$  to arterial tracer concentrations (48) was used together with the parameters listed in Ref. 43. In this study, the same AIF was applied to both  $R_2^*$ - and  $R_2$ -based perfusion data. SE images cannot be used for correct AIF determination due to their insensitivity to large vessels (17,18) and due to flow-related signal voids, which are caused by the relatively long period of time between signal excitation and signal refocusing.

Careful AIF selection was required, as the time courses of the EPI images measured at  $TE_2 = 34.1$  ms often showed signal saturation artifacts at the peak of the bolus passage (49,50), caused by high Gd concentrations in arteries that lead to a complete dephasing of the MRI signals before their readout. Signal saturation at the peak of the bolus passage causes errors in the determination of  $R_2^*$ ; hence, it leads to distortions in the shape of the AIF. To prevent AIF selection within voxels affected by signal saturation, the time courses of the GE signals acquired at  $TE_1$  and  $TE_2$  were analyzed. Voxels in which at least one of the GE signals was too close to the noise floor at the peak of the bolus passage were excluded from the pool of AIF candidate voxels. In the current implementation, this approach was performed manually and may be user dependent. However, for automatic AIF selection approaches, an additional criterion could be the exclusion of voxels in which the GE signal acquired

at  $TE_1$  or  $TE_2$  is smaller than twice the standard deviation of the corresponding prebolus signal.

An AIF was selected in close proximity to the blood vessel, but not within the vessel. This approach was justified by the results of a recently published study by Bleeker et al. (51) in which the authors concluded that a voxel completely outside of the blood vessel should be selected for AIF determination. This approach together with a  $T_1$ -independent multiecho fit assured a correct shape of the selected AIF.

### AIF Scaling

CBF and CBV values were scaled using a venous output function (VOF), which was obtained from multiecho,  $R_2^*$ -based tracer concentrations within the superior sagittal sinus. Scaling was performed in a similar way as shown in (42), using an arterial-venous scaling factor  $k_{av}$ . Because of very large venous tracer concentrations, signal saturation, also referred to as “clipping”, occurred in most VOF candidate voxels during the peak of the bolus passage. Therefore, to prevent errors caused by saturated MRI signal curves, the scaling factor  $k_{av}$  was based on postbolus venous and arterial tracer concentrations only.

Corrected CBF and CBV were determined from the multiplication of the proportionality constant  $k_{av}$  with the noncorrected CBF and CBV estimates, referred to as  $CBF_{NC}$  and  $CBV_{NC}$ .  $k_{av}$  was derived from the ratio of the integrals of the AIF and VOF curves using all time points following the end of the first pass of the contrast agent through the brain. Thus,

$$k_{av} = \frac{\int_{t=t_e}^{t_n} c_a(t) dt}{\int_{t=t_e}^{t_n} c_v(t) dt} \quad [7]$$

and

$$\begin{aligned} CBF &= CBF_{NC} \cdot k_{av} \\ CBV &= CBV_{NC} \cdot k_{av} \end{aligned} \quad [8]$$

Here,  $t_e$  is the first time point following the end of the first pass of the contrast agent,  $t_n$  is the last time point acquired in the dynamic imaging series, and  $c_a(t)$  and  $c_v(t)$  represent the arterial and venous contrast agent concentrations, respectively.

## RESULTS

Figure 2a shows images of all five echoes of a specified slice in a selected patient, obtained during the prebolus baseline period and at the time when the peak of the bolus was passing through the capillary bed. The signal drop associated with the contrast agent passage is clearly visible in all five echo images. The time curve of each echo within a typical voxel in tissue is shown in Fig. 2b. In close agreement with the simulations shown in Ref. 17, contrast agent-induced signal changes were much larger in GE images (acquired at  $TE_1$  and  $TE_2$ ) than in the SE image acquired at  $TE_5$ . Overall, the largest changes in signal amplitude were seen in the GE images acquired at  $TE_2 = 34.1$  ms.  $TE_2$  is within the range of typical echo times used for single-echo GE-PWI



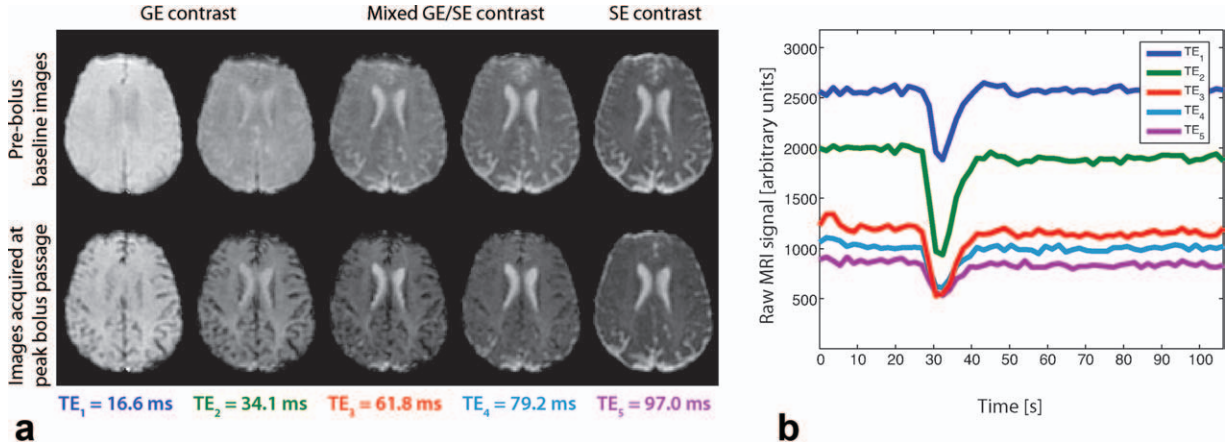


FIG. 2. **a**: EPI images in a selected patient acquired during baseline (top row) and at the peak of the bolus passage (bottom row) in a SAGE PWI experiment. This figure shows images of all five echo trains in a five-echo SAGE EPI acquisition using the parameters listed in Table 1. **b**: MRI signal time course of each EPI train in a specified voxel within gray matter. Note that the largest contrast agent-induced signal drop occurred in the EPI images acquired at  $TE_2 = 34.1$  ms, a typical echo time for GE-PWI experiments at 3 T. [Color figure can be viewed in the online issue, which is available at [wileyonlinelibrary.com](http://wileyonlinelibrary.com).]

acquisitions at 3 T. Note that each of the five individual echoes could be used to compute perfusion parameters. However, we based the perfusion maps in this study on the time courses of  $R_2$  and  $R_2^*$ , and, for comparative purposes, on the second echo images acquired at  $TE_2$  and the fifth echo images acquired at  $TE_5$ .

Figure 3a demonstrates the time courses of a manually selected AIF and VOF in the same patient shown in Fig. 2, based on the second EPI train acquired at  $TE_2 = 34.1$  ms. The VOF suffered from substantial  $T_1$ -shortening effects, resulting in an initial dip and a postbolus drop in the apparent venous tracer concentration, both leading to physically impossible negative values.  $T_1$  effects also reduced postbolus AIF values. In contrast, the time courses of multiecho  $R_2^*$ -based AIF (cf. Fig. 3b) and VOF (cf. Fig. 3c) yielded increased postbolus tracer concentrations. Although the selected multiecho AIF did not suffer from saturation artifacts, the multiecho fitted VOF did, causing erroneous tracer concentrations during the

first pass of the bolus through the brain. However, after the end of the first bolus passage, VOF clipping ceased, resulting in elevated postbolus tracer concentrations, which represent residual Gd in the blood stream. In this study, it was important that the postbolus VOF was accurate, because it was used to determine the AIF scaling factor  $k_{av}$ .

Figure 4 shows CBF and CBV maps in a patient with subacute stroke. These maps were processed using  $R_2^*$ - and  $R_2$ -based tracer concentrations, as well as tracer concentrations obtained from single-echo GE images acquired at  $TE_2 = 34.1$  ms and single-echo SE images acquired at  $TE_5 = 97.0$  ms. Large-vessel blooming can be seen on both GE- and  $R_2^*$ -based DSC-PWI maps. In contrast, both SE- and  $R_2$ -based DSC-PWI maps were mostly free from large-vessel blooming due to their restricted sensitivity to smaller vessels. In Fig. 5, histograms of CBF and CBV verified the increased macrovascular sensitivity of GE- and  $R_2^*$ -based perfusion data when

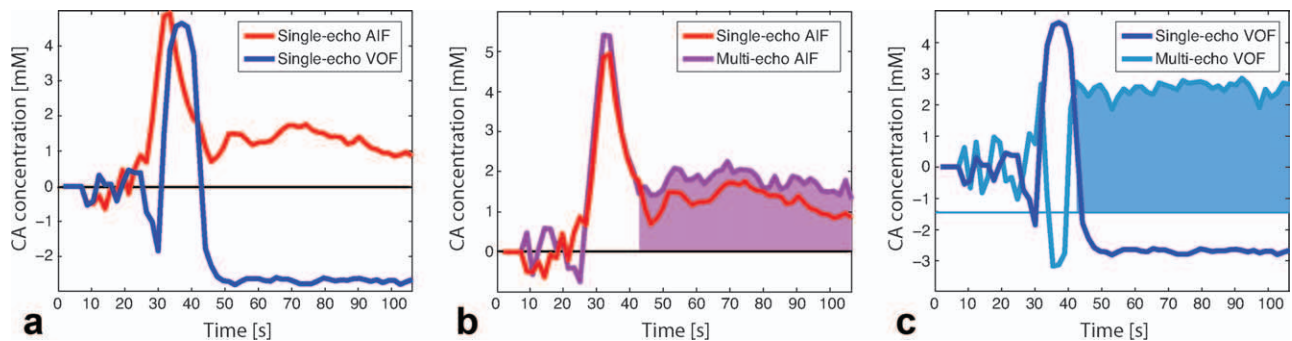


FIG. 3. **a**: Single-echo AIF (red) and VOF (blue), both calculated from the GE EPI time course acquired at  $TE_2 = 34.1$  ms. The presence of  $T_1$ -shortening effects caused an underestimation of contrast agent concentration in the VOF, visible at the onset of the first bolus passage and during the postbolus period. The AIF was also affected by  $T_1$  effects, but to a lesser extent. **b**: Comparison of single-echo AIF (red) with multiecho AIF (purple). The multiecho AIF was corrected for  $T_1$ -shortening effects, with the result of elevated postbolus contrast agent concentrations, reflecting residual Gd in the blood stream. **c**: Single-echo VOF (blue) vs. multiecho VOF (cyan). The multiecho fitted VOF was corrected for  $T_1$ -induced negative contrast agent concentrations. However, during the first passage of the bolus, the multiecho VOF experienced signal saturation, resulting in incorrect  $R_2^*$  estimations. Therefore, for quantitative DSC-PWI, AIF scaling was based on the postbolus levels of the multiecho fitted AIF (purple area under the concentration curve) and the multiecho fitted VOF (cyan). [Color figure can be viewed in the online issue, which is available at [wileyonlinelibrary.com](http://wileyonlinelibrary.com).]

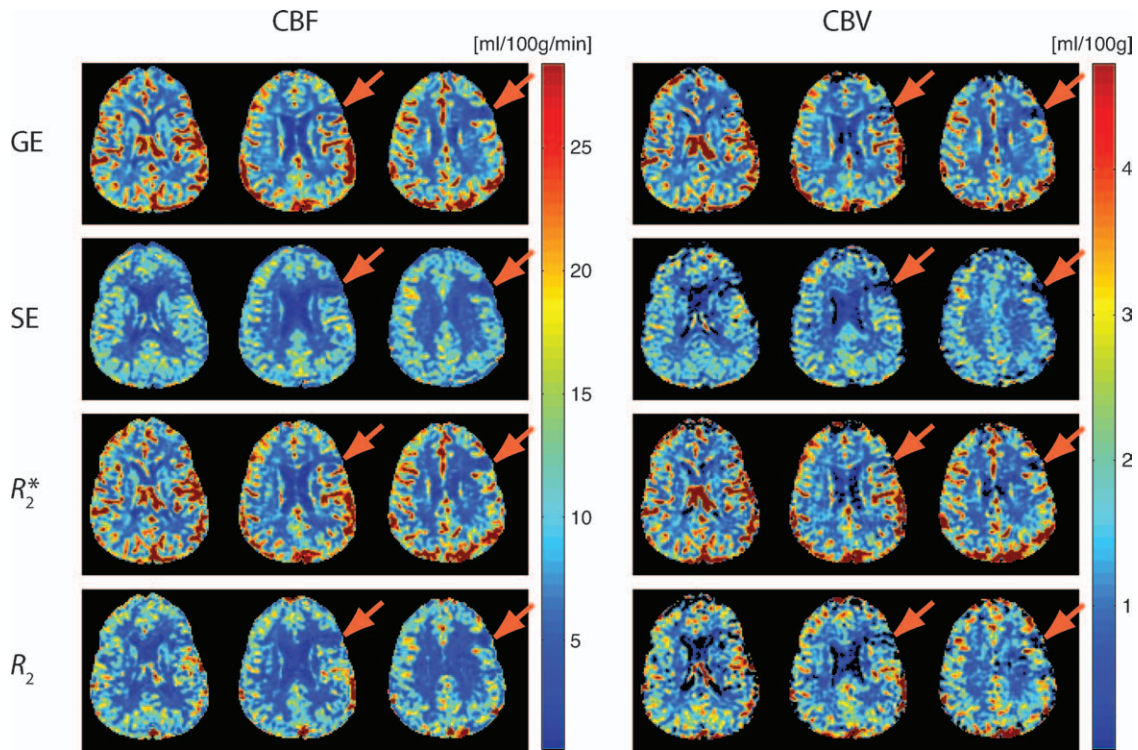


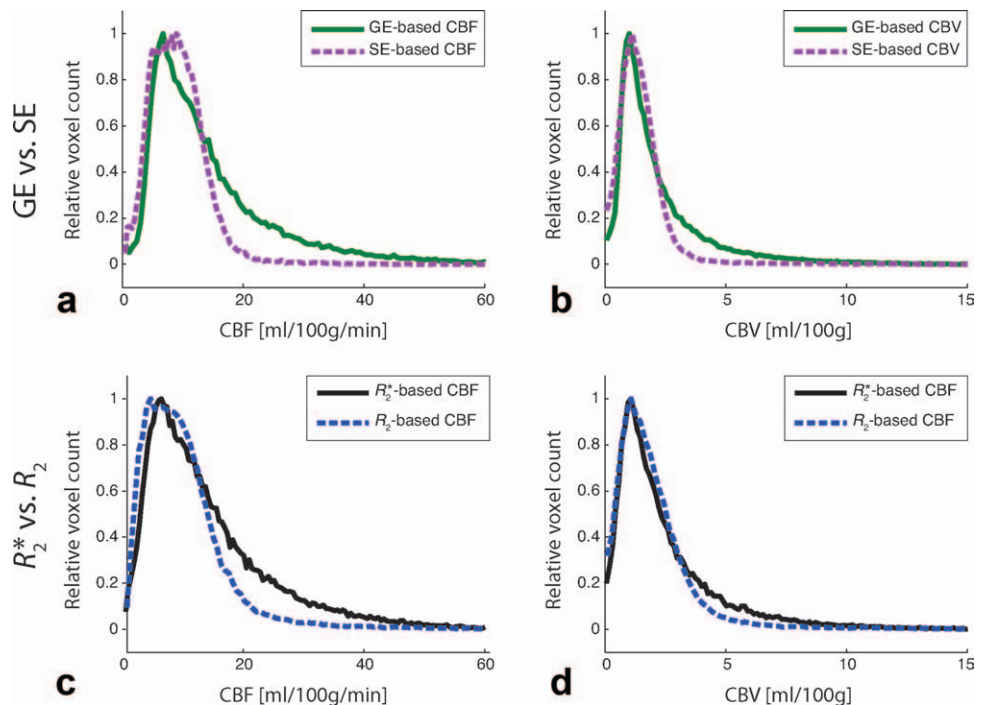
FIG. 4. Comparison of GE-, SE-,  $R_2^*$ -, and  $R_2$ -based CBF and CBV in a 63-year-old patient with subacute stroke in the left frontal cortex. Both SE-PWI and  $R_2$ -based DSC-PWI resulted in considerably decreased large vessel blooming seen on GE- and  $R_2^*$ -based maps, leading to a better visibility of the lesion (arrows). [Color figure can be viewed in the online issue, which is available at [wileyonlinelibrary.com](http://wileyonlinelibrary.com).]

compared with SE- and  $R_2$ -based data. These histograms demonstrated a narrow distribution of CBF and CBV in case of SE- and  $R_2$ -based data, whereas GE- and  $R_2^*$ -based data resulted in a broader distribution of CBF and CBV, indicating substantial contributions from larger vessels in voxels with increased blood flow and blood volume.

These results are in good agreement with simulations performed elsewhere (16,17).

Figure 6 represents a case of subacute left posterior middle cerebral artery infarct with considerable BBB leakage and a potential for errors caused by  $T_1$ -shortening effects. Although GE-PWI and SE-PWI yielded CBV

FIG. 5. Histograms of (a, c) CBF and (b, d) CBV values for the patient shown in Fig. 4, processed using (a, b) single-echo data and (c, d) multiecho data. In the absence of substantial BBB leakage, the histograms showed similarities between GE- and  $R_2^*$ -based DSC-PWI data as well as between SE- and  $R_2$ -based data. The narrower SE- and  $R_2$ -based distributions of CBF and CBV confirmed a decreased sensitivity to larger blood vessels. [Color figure can be viewed in the online issue, which is available at [wileyonlinelibrary.com](http://wileyonlinelibrary.com).]





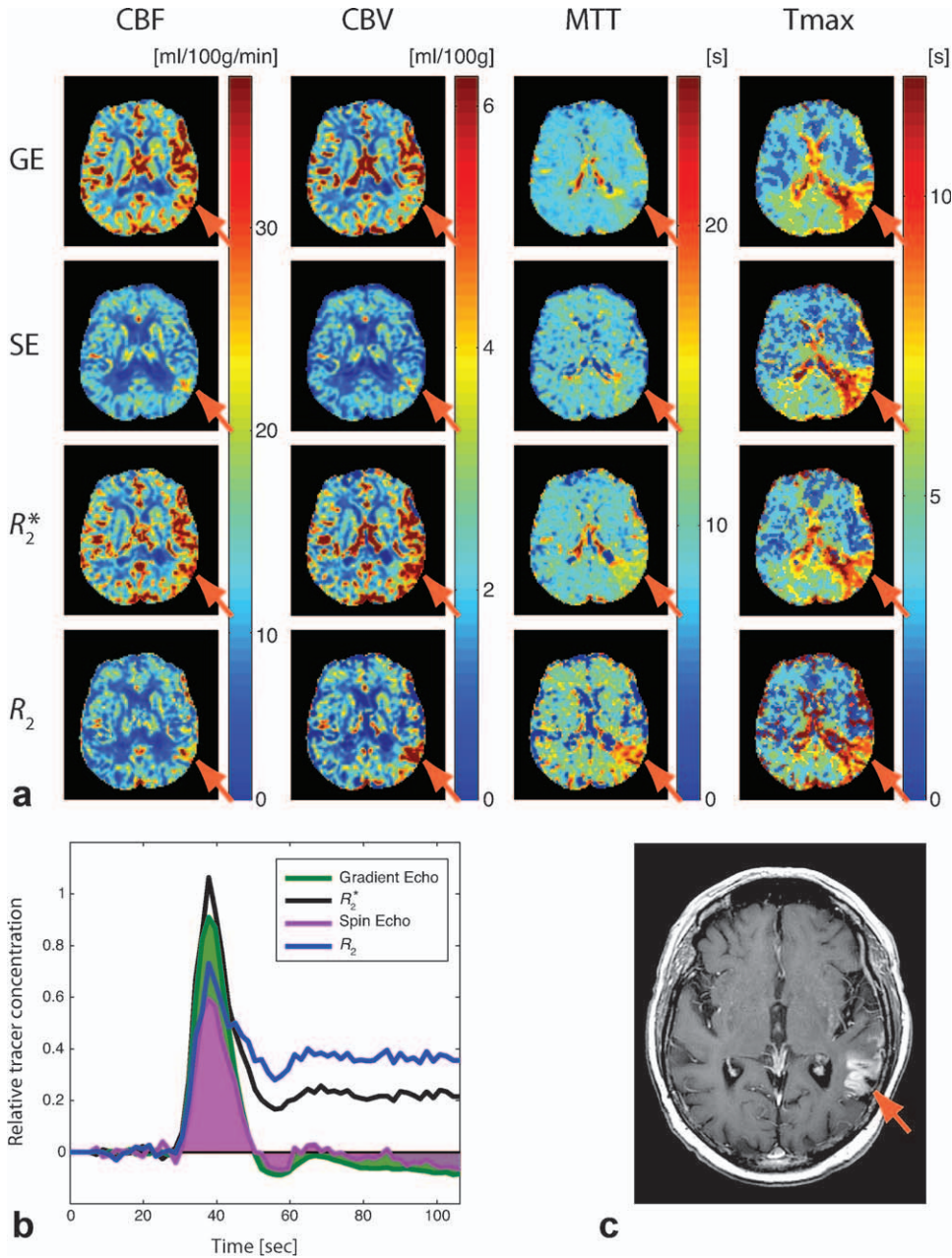


FIG. 6. **a**: Comparison of GE-, SE-,  $R_2^*$ -based, and  $R_2$ -based DSC-PWI maps in a patient with subacute infarct in the territory of the left posterior middle cerebral artery.  $R_2^*$ - and  $R_2$ -based maps resulted in elevated CBV in the region where the stroke had occurred. This effect is less evident on single-echo GE and SE CBV maps.  $R_2^*$  and  $R_2$ -based data yielded an associated increase in MTT, particularly well defined in  $R_2$ -based maps. In contrast, single-echo MTT maps resulted in a decrease in the ischemic region.  $T_{max}$  maps were similar among all methods used. **b**: Tracer concentration vs. time in the ischemic region. GE and SE tracer concentration curves dropped below baseline, resulting in apparent CBV decrease (the calculated CBV is equivalent to the areas under the green (GE CBV) and purple (SE CBV) concentration curves). **c**: A  $T_1$ -weighted postcontrast image shows BBB leakage.

values in areas with BBB leakage that were similar to those of the surrounding tissue (see arrows in Fig. 6a),  $R_2^*$ - and  $R_2$ -based DSC-PWI resulted in considerably increased CBV in the ischemic region, reflecting an increase in local contrast agent concentration associated with leakage. Although  $R_2^*$ - and  $R_2$ -based CBV maps correctly reflected local contrast agent concentrations, these maps were not confined to the intravascular space in the presence of BBB leakage. However, the resulting CBV maps can be used in more advanced perfusion models that separate signal dephasing effects arising from intravascular and extravascular Gd molecules. In contrast to CBV,  $R_2^*$ - and GE-based DSC-PWI as well as  $R_2$ - and SE-based DSC-PWI resulted in comparable CBF. As a consequence of the central volume principle that relates MTT to the ratio of CBV and CBF, MTT differed substantially in the region affected by the stroke, whereas  $T_{max}$  was

almost the same for all four methods (52). Tracer concentrations showing differences between the four methods are plotted in Fig. 6b. A postcontrast  $T_1$ -weighted image (Fig. 6c) confirmed the presence of the BBB leakage.

In Fig. 7, a patient with diagnosed glioblastoma multiforme is presented. SAGE PWI data were acquired following tumor resection and radiation therapy. On SAGE PWI data as well as on postcontrast  $T_1$ -weighted GE images, a region of new enhancement was found posterior to the surgical resection cavity.  $R_2^*$ - and  $R_2$ -based maps showed an increased CBV in this region, whereas SE-based CBV was comparable to the surrounding tissue and GE-based CBV was only slightly elevated. A closer look at the tracer concentration curves (Fig. 7d) revealed substantial contrast agent extravasation, resulting in negative postbolus tracer concentrations for GE and SE data, whereas  $R_2^*$ - and  $R_2$ -based contrast agent concentrations

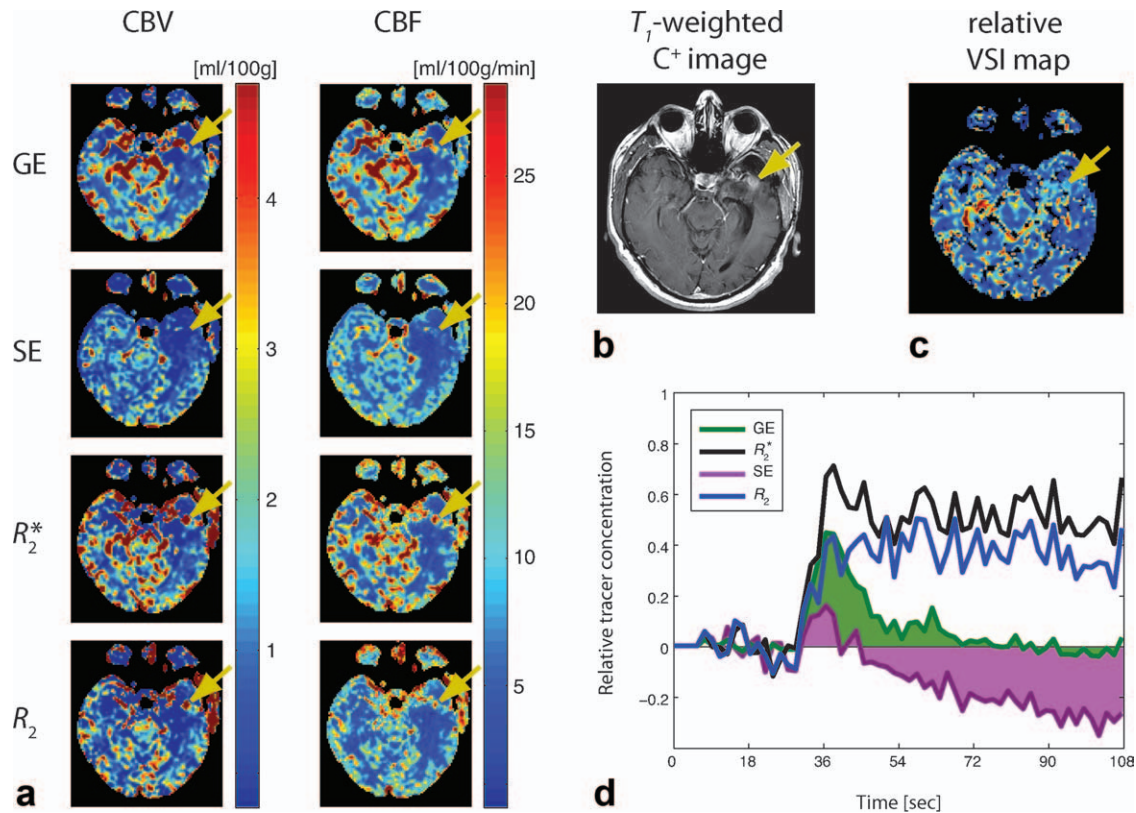


FIG. 7. Patient with glioblastoma multiforme, status postresection and radiation therapy. An area of new contrast enhancement is seen on  $R_2^*$ - and  $R_2$ -based CBV maps (a) as well as on a  $T_1$ -weighted postcontrast image (b). The new enhancement is also visible to a limited extent on GE CBV, but not on SE CBV data. CBF is shown for comparative purposes, indicating slightly elevated flow in this region. c: A VSI map shows a slightly increased vessel radius, suggesting active tumor progression. d: Tracer concentration curves confirm a substantial contrast agent uptake, seen on  $R_2^*$ - and  $R_2$ -based data (black and blue curves, respectively). In contrast, GE- and SE-data show reduced postbolus concentrations below baseline levels, leading to a reduction in apparent CBV [SE data with substantial negative CBV contributions (purple) and GE data with slightly negative contributions (green)]. [Color figure can be viewed in the online issue, which is available at [wileyonlinelibrary.com](http://wileyonlinelibrary.com).]

remained above prebolus baseline levels. A vessel size image of the same slice is shown in Fig. 7c, demonstrating slightly elevated average vessel radii within this region. Again,  $R_2^*$ - and  $R_2$ -based CBV maps using standard tracer kinetic modeling cannot separate extravascular from intravascular contributions. Thus, these maps represent the total volume of distribution of the contrast agent rather than intravascular CBV.

## DISCUSSION

In this study, we described the combined acquisition of time-resolved  $R_2^*$ - and  $R_2$ -based MRI data, facilitated by a parallel imaging-accelerated multiecho spin- and gradient-echo EPI pulse sequence, and we showed its application to measurements of cerebral perfusion parameters. The presented method, referred to as SAGE PWI, combined the advantages of both GE- and SE-based DSC-PWI in a single pulse sequence, and it preserved the option to extract single-echo GE-PWI maps, which are still the first choice for routine clinical DSC-PWI exams. Thus, SAGE PWI facilitates a direct comparison with conventional GE DSC-PWI.

Our observations in this study indicated that the perfusion maps provided by  $R_2$ -based DSC-PWI and SE-PWI

could be diagnostically more relevant than  $R_2^*$ -based DSC-PWI maps and GE-PWI maps for the interpretation of the status of tissue microperfusion in cerebrovascular diseases. The selective sensitivity of  $R_2$ -based and SE-PWI maps to the microvasculature improved the visibility of smaller infarcts (cf. Fig. 4). However, the overall sensitivity to the presence of contrast agent was higher with  $R_2^*$ -GE-based DSC-PWI than with  $R_2$ -SE-based DSC-PWI, as demonstrated in Fig. 2b. Moreover, GE-based DSC-PWI methods allow direct AIF determination, which is necessary for deconvolution-based CBF computation and quantitative DSC-PWI. In contrast, AIF determination based on SE data is difficult and prone to errors. With SAGE EPI, direct AIF determination facilitated the computation of quantitative perfusion parameters with both GE- and SE-contrast, presenting a big advantage of SAGE PWI over single-echo SE- or GE-based DSC-PWI.

The use of multiecho data to determine contrast agent concentrations in brain tissue eliminated  $T_1$ -shortening effects, a particular issue in the presence of BBB leakage. If  $T_1$  effects are unaccounted for, the accuracy of DSC-PWI maps is limited, as shown in (24). However, in the absence of contrast agent leakage, such as for the stroke patient shown in Fig. 4, errors arising from  $T_1$ -shortening effects were small. Thus, GE- and  $R_2^*$ -based DSC-PWI



maps on one hand and SE- and  $R_2$ -based DSC-PWI data on the other hand were fairly similar, as shown in Fig. 5 in histograms of CBF and CBV. However, if BBB leakage was present, such as in tumors or cases of subacute stroke, GE- and SE-based DSC-PWI parameters were erroneous. We demonstrated in a patient with a subacute stroke that both GE- and SE-based postbolus tracer concentrations dropped below baseline, caused by contrast agent extravasation and subsequent tissue  $T_1$  shortening (cf. Fig. 6). This effect reduced apparent CBV, which was derived from the integration of the contrast agent concentration time curve in each voxel. In contrast,  $T_1$ -shortening effects affected the peak of the residue function from which CBF was derived to a limited extent only. Hence, because of the central volume principle, MTT was too short in GE- and SE-based data. In fact, the MTT values in the ischemic region were even lower than normal physiological MTT, indicating that both GE-PWI and SE-PWI were confounded by  $T_1$ -shortening effects. In contrast, DSC-PWI maps derived from  $T_1$ -independent  $R_2^*$  and  $R_2$  estimates resulted in an increase in tracer concentrations associated with BBB leakage, and thus in elevated CBV and MTT, but unchanged CBF. Regardless of the method that was used,  $T_{\max}$  remained elevated in the region of the subacute stroke. Thus, our results showed that  $R_2^*$ - and  $R_2$ -based DSC-PWI maps resulted in a better spatial match between perfusion abnormalities expressed via MTT and  $T_{\max}$  when compared with GE-PWI and SE-PWI data.

For the tumor case shown in Fig. 7, the attending radiologist attributed the enhancement seen on postcontrast  $T_1$ -weighted images to radiation necrosis or tumor progression, without ruling out either possibility.  $R_2^*$ - and  $R_2$ -based DSC-PWI data yielded an elevated CBV in the area posterior to the tumor resection cavity, caused by contrast agent extravasation. This effect was not seen on SE-PWI data, and it was less prominent on GE-PWI data.  $R_2^*$ - and  $R_2$ -based CBF maps demonstrated slightly elevated blood flow in the questioned area, again not seen on SE data, and only revealed to a limited extent on GE data. In addition, a VSI map indicated the presence of increased large vessel supply. Therefore, rather than being radiation necrosis, it was more likely that in this patient the tumor had recurred, which led to the elevated CBF and CBV seen on our data acquired with SAGE EPI. As with the stroke case presented in Fig. 6, elevated tracer concentrations could be detected in  $R_2^*$ - and  $R_2$ -based DSC-PWI only, whereas GE- and SE-based DSC-PWI resulted in an underestimation of CBV in areas of BBB leakage. Thus, Fig. 7 exemplified a case in which SAGE PWI added additional information for the patient assessment, with the potential to increase the accuracy of the clinical diagnosis.

Please note that the use of standard tracer kinetic modeling with SAGE PWI could result in CBV overestimation in areas of considerable BBB leakage. Although this does not necessarily reflect errors in the determination of total contrast agent concentrations, the resulting CBV is not confined to the intravascular space, but may include the extracellular space in parts. More advanced perfusion models would be able to separate intravascular from extravascular contributions in computed CBV; however,

in this study, we based our calculations on standard intravascular tracer kinetic models. BBB leakage is a serious concern in many cerebrovascular diseases; thus, its detection adds important information to DSC-PWI exams. As shown in this study, the disregard of  $T_1$ -shortening effects when using standard GE-PWI imaging causes CBV underestimation, potentially resulting in clinical misinterpretation of DSC-PWI data due to the lack of BBB leakage detection.

A multiecho fitted AIF was determined in this study to facilitate absolute perfusion quantification. This approach is compensated for  $T_1$ -shortening effects (29), whereas a single-echo AIF could lead to  $T_1$ -induced quantification errors. Simulations performed on varying AIF shapes (data not shown) revealed differences in absolute CBV of up to 100%, caused by differences in postbolus arterial tracer concentrations between an uncompensated AIF and a  $T_1$ -compensated multiecho fitted AIF (cf. Fig. 3b), underlining the importance of  $T_1$  correction for quantitative DSC-PWI. With a multiecho fit of the VOF, in contrast to a carefully selected AIF, signal saturation artifacts were induced, which led to incorrect VOF shapes during the first pass of the contrast agent through the brain tissue (cf. Fig. 3c). The cause of these saturation artifacts was large tracer concentrations within the superior sagittal sinus during the peak of the bolus passage, with the result of very low signal magnitudes in images acquired at TE<sub>2</sub>. However, a single-echo approach for VOF determination would be prone to errors caused by  $T_1$ -shortening effects arising from previously excited spins that experience increased longitudinal excitation relaxation in proximity to Gd molecules. In consequence, venous contrast concentrations could drop below baseline after the first bolus passage and lead to physically impossible negative concentration values (see Fig. 3c), thus preventing correct VOF-based AIF scaling. Therefore, in this study, we suggested AIF scaling based on the time courses of the multiecho fitted AIF and VOF following the end of the first bolus passage. With this method, VOF clipping artifacts and  $T_1$ -shortening effects were eliminated.

It should be noted that  $T_1$ -shortening effects affecting the GE-PWI data shown here might be slightly more pronounced compared to conventional GE-PWI data. This is due to the fact that a 90° excitation pulse was used in SAGE EPI, in contrast to lower flip angles typically used in GE-based DSC-PWI. However, with a  $T_1$ -independent approach, such as with SAGE EPI, the presence of increased  $T_1$ -shortening effects caused by a 90° excitation flip angle does not affect  $R_2$ - and  $R_2^*$ -based DSC-PWI data. Moreover, there is limited flexibility with the chosen flip angles in combined GE and SE sequences, and a 90° excitation pulse results in increased signal-to-noise ratios in SE data.

In this study, we assumed that the ratio of the relaxivity constants  $x_1$  and  $x_2$  was 1:4.25. This value was based on the average ratio of the  $R_2$ -based CBF to the  $R_2^*$ -based CBF in white matter. It is in good agreement to computations shown in Ref. 15. However, the validity of this proportionality requires further investigation: the relationship between changes in  $R_2$  and contrast agent concentration is found to be nonlinear (17,53). Thus, the assumption of a linear relationship between these values could induce quantification errors in  $R_2$ -based DSC-PWI

and SE-PWI. A potential correction for nonlinear effects would include the evaluation of the relationship between  $R_2$ - and  $R_2^*$ -based CBF to CBF based on quantitative ASL data acquired in a separate measurement (54). However, this comparison was not done for this study.

## CONCLUSIONS

SAGE EPI facilitates the simultaneous acquisition of  $R_2^*$ - and  $R_2$ -based perfusion data for quantitative,  $T_1$ -independent GE and SE DSC-PWI analysis, allowing a more differentiated clinical diagnosis, facilitated by a single acquisition. Although the overall sensitivity of GE perfusion data to the contrast agent passage is superior to SE data, SE-based DSC-PWI measurements show results that are more specific to the microvasculature. Therefore, SE-PWI might improve the visibility of hypoperfused regions otherwise hidden or confounded by larger blood vessels. Furthermore, it might reduce the risk of mimicking normal or even increased perfusion in situations with no actual microvascular perfusion, such as in the presence of capillary shunting.

SAGE PWI merges the advantages of higher specificity to the microvasculature of pure SE-based DSC-PWI methods with the possibility of a direct AIF determination and higher overall sensitivity to the presence of contrast agent of GE-based DSC-PWI techniques. Moreover, SAGE PWI facilitates VSI without additional acquisition time, and it even allows the calculation of the oxygen extraction fraction of brain tissue (55), turning SAGE PWI into a compact pulse sequence for the assessment of cerebrovascular diseases.

## REFERENCES

- Villringer A, Rosen BR, Belliveau JW, Ackerman JL, Lauffer RB, Buxton RB, Chao YS, Wedeen VJ, Brady TJ. Dynamic imaging with lanthanide chelates in normal brain: contrast due to magnetic susceptibility effects. *Magn Reson Med* 1988;6:164–174.
- Edelman RR, Mattle HP, Atkinson DJ, Hill T, Finn JP, Mayman C, Ronthal M, Hoogewoud HM, Kleefeld J. Cerebral blood flow: assessment with dynamic contrast-enhanced  $T_2^*$ -weighted MR imaging at 1.5 T. *Radiology* 1990;176:211–220.
- Rosen BR, Belliveau JW, Vevea JM, Brady TJ. Perfusion imaging with NMR contrast agents. *Magn Reson Med* 1990;14:249–265.
- Rosen BR, Belliveau JW, Buchbinder BR, McKinsty RC, Porkka LM, Kennedy DN, Neuder MS, Fisel CR, Aronen HJ, Kwong KK, Weisskoff RM, Cohen MS, Brady TJ. Contrast agents and cerebral hemodynamics. *Magn Reson Med* 1991;19:285–292.
- Guckel F, Brix G, Rempp K, Deimling M, Rother J, Georgi M. Assessment of cerebral blood volume with dynamic susceptibility contrast enhanced gradient-echo imaging. *J Comput Assist Tomogr* 1994;18:344–351.
- Rother J, Guckel F, Neff W, Schwartz A, Hennerici M. Assessment of regional cerebral blood volume in acute human stroke by use of single-slice dynamic susceptibility contrast-enhanced magnetic resonance imaging. *Stroke* 1996;27:1088–1093.
- Nighoghossian N, Berthezene Y, Philippon B, Adeleine P, Froment JC, Trouillas P. Hemodynamic parameter assessment with dynamic susceptibility contrast magnetic resonance imaging in unilateral symptomatic internal carotid artery occlusion. *Stroke* 1996;27:474–479.
- Sorensen AG, Copen WA, Ostergaard L, Buonanno FS, Gonzalez RG, Rordorf G, Rosen BR, Schwamm LH, Weisskoff RM, Koroshetz WJ. Hyperacute stroke: simultaneous measurement of relative cerebral blood volume, relative cerebral blood flow, and mean tissue transit time. *Radiology* 1999;210:519–527.
- Shih LC, Saver JL, Alger JR, Starkman S, Leary MC, Vinuela F, Duckwiler G, Gobin YP, Jahan R, Villablanca JP, Vespa PM, Kidwell CS. Perfusion-weighted magnetic resonance imaging thresholds identifying core, irreversibly infarcted tissue. *Stroke* 2003;34:1425–1430.
- Albers GW, Thijs VN, Wechsler L, Kemp S, Schlaug G, Skalabrini E, Bammer R, Kakuda W, Lansberg MG, Shuaib A, Coplin W, Hamilton S, Moseley M, Marks MP. Magnetic resonance imaging profiles predict clinical response to early reperfusion: the diffusion and perfusion imaging evaluation for understanding stroke evolution (DEFUSE) study. *Ann Neurol* 2006;60:508–517.
- Maeda M, Itoh S, Kimura H, Iwasaki T, Hayashi N, Yamamoto K, Ishii Y, Kubota T. Tumor vascularity in the brain: evaluation with dynamic susceptibility-contrast MR imaging. *Radiology* 1993;189:233–238.
- Aronen HJ, Gazit IE, Louis DN, Buchbinder BR, Pardo FS, Weisskoff RM, Harsh GR, Cosgrove GR, Halpern EF, Hochberg FH. Cerebral blood volume maps of gliomas: comparison with tumor grade and histologic findings. *Radiology* 1994;191:41–51.
- Donahue KM, Krouwer HG, Rand SD, Pathak AP, Marszalkowski CS, Censky SC, Prost RW. Utility of simultaneously acquired gradient-echo and spin-echo cerebral blood volume and morphology maps in brain tumor patients. *Magn Reson Med* 2000;43:845–853.
- Tropes I, Grimaud S, Vaeth A, Grillon E, Julien C, Payen JF, Lamalle L, Decorps M. Vessel size imaging. *Magn Reson Med* 2001;45:397–408.
- Kiselev VG, Strecker R, Ziyeh S, Speck O, Hennig J. Vessel size imaging in humans. *Magn Reson Med* 2005;53:553–563.
- Weisskoff RM, Zuo CS, Boxerman JL, Rosen BR. Microscopic susceptibility variation and transverse relaxation: theory and experiment. *Magn Reson Med* 1994;31:601–610.
- Boxerman JL, Hamberg LM, Rosen BR, Weisskoff RM. MR contrast due to intravascular magnetic susceptibility perturbations. *Magn Reson Med* 1995;34:555–566.
- Speck O, Chang L, DeSilva NM, Ernst T. Perfusion MRI of the human brain with dynamic susceptibility contrast: gradient-echo versus spin-echo techniques. *J Magn Reson Imaging* 2000;12:381–387.
- Ames A III, Wright RL, Kowada M, Thurston JM, Majno G. Cerebral ischemia. II. The no-reflow phenomenon. *Am J Pathol* 1968;52:437–453.
- del Zoppo GJ, Mabuchi T. Cerebral microvessel responses to focal ischemia. *J Cereb Blood Flow Metab* 2003;23:879–894.
- Bandettini PA, Wong EC, Jesmanowicz A, Hinks RS, Hyde JS. Simultaneous mapping of activation-induced  $\Delta R_2^*$  and  $\Delta R_2$  in the human brain using a combined gradient-echo and spin-echo EPI pulse sequence. In: *Proceedings of the 12th Annual Meeting of SMRM*, New York, NY, USA; 1993. p 169.
- Schminda KM, Rand SD, Joseph AM, Lund R, Ward BD, Pathak AP, Ulmer JL, Badruddoja MA, Krouwer HG. Characterization of a first-pass gradient-echo spin-echo method to predict brain tumor grade and angiogenesis. *AJNR Am J Neuroradiol* 2004;25:1524–1532.
- Levin JM, Wald LL, Ross MH, Kaufman MJ, Cohen BM, Renshaw PF. Investigation of T1 effects as basis for residual contrast agent effects seen in sequential dynamic susceptibility contrast experiments. In: *Proceedings of the 4th Annual Meeting of SMRM*, New York, NY, USA; 1996. p 441.
- Calamante F, Vonken EJ, van Osch MJ. Contrast agent concentration measurements affecting quantification of bolus-tracking perfusion MRI. *Magn Reson Med* 2007;58:544–553.
- Wintermark M, Albers GW, Alexandrov AV, Alger JR, Bammer R, Baron JC, Davis S, Demaerschalk BM, Derdeyn CP, Donnan GA, Eastwood JD, Fiebach JB, Fisher M, Furie KL, Goldmakher GV, Hacke W, Kidwell CS, Kloska SP, Kohrmann M, Koroshetz W, Lee TY, Lees KR, Lev MH, Liebeskind DS, Ostergaard L, Powers WJ, Provenzale J, Schellinger P, Silbergleit R, Sorensen AG, Wardlaw J, Wu O, Warach S. Acute stroke imaging research roadmap. *Stroke* 2008;39:1621–1628.
- Weisskoff RM, Boxerman JL, Sorensen AG, Kulke SF, Campbell TA, Rosen BR. Simultaneous blood volume and permeability mapping using a single Gd-based contrast injection. In: *Proceedings of the 2nd Annual Meeting of SMRM*, San Francisco, CA, USA; 1994. p 279.
- Sorensen AG, Reimer P. Cerebral MR perfusion imaging. Stuttgart/New York: Georg Thieme Verlag; 2000.
- Vonken EJ, van Osch MJ, Bakker CJ, Viergever MA. Measurement of cerebral perfusion with dual-echo multi-slice quantitative dynamic susceptibility contrast MRI. *J Magn Reson Imaging* 1999;10:109–117.
- Newbould RD, Skare ST, Jochimsen TH, Alley MT, Moseley ME, Albers GW, Bammer R. Perfusion mapping with multiecho multishot parallel imaging EPI. *Magn Reson Med* 2007;58:70–81.
- Paulson ES, Schminda KM. Comparison of dynamic susceptibility-weighted contrast-enhanced MR methods: recommendations for measuring relative cerebral blood volume in brain tumors. *Radiology* 2008;249:601–613.

31. Schmiedeskamp H, Straka M, Bammer R. Compensation of slice profile mismatch in combined spin- and gradient-echo EPI pulse sequences. *Magn Reson Med*, in press.
32. Newbould RD, Skare S, Albers G, Bammer R. Simultaneous T2 and T2\* dynamic susceptibility contrast perfusion imaging using a multi-echo parallel imaging approach. In: *Proceedings of the Joint Annual Meeting of ISMRM/ESMRMB*, Berlin, Germany; 2007. p 1451.
33. Le Roux P. Exact synthesis of radiofrequency waveforms. In: *Proceedings of the 7th Annual Meeting of SMRM*, San Francisco, CA, USA; 1988. p 1049.
34. Shinnar M, Bolinger L, Leigh JS. The synthesis of soft pulses with a specified frequency response. *Magn Reson Med* 1989;12:88–92.
35. Shinnar M, Bolinger L, Leigh JS. The use of finite impulse response filters in pulse design. *Magn Reson Med* 1989;12:81–87.
36. Shinnar M, Eleff S, Subramanian H, Leigh JS. The synthesis of pulse sequences yielding arbitrary magnetization vectors. *Magn Reson Med* 1989;12:74–80.
37. Shinnar M, Leigh JS. The application of spinors to pulse synthesis and analysis. *Magn Reson Med* 1989;12:93–98.
38. Pauly J, Le Roux P, Nishimura D, Macovski A. Parameter relations for the Shinnar-Le Roux selective excitation pulse design algorithm [NMR imaging]. *IEEE Trans Med Imaging* 1991;10:53–65.
39. Skare S, Clayton D, Newbould R, Moseley M, Bammer R. A fast and robust minimum entropy based ghost correction. In: *Proceedings of the 14th Annual Meeting of the ISMRM*, Seattle, WA, USA; 2006. p 2349.
40. Griswold MA, Jakob PM, Heidemann RM, Nittka M, Jellus V, Wang J, Kiefer B, Haase A. Generalized autocalibrating partially parallel acquisitions (GRAPPA). *Magn Reson Med* 2002;47:1202–1210.
41. Qu P, Shen GX, Wang C, Wu B, Yuan J. Tailored utilization of acquired k-space points for GRAPPA reconstruction. *J Magn Reson* 2005;174:60–67.
42. Straka M, Albers GW, Bammer R. Real-time diffusion-perfusion mismatch analysis in acute stroke. *J Magn Reson Imaging* 2010;32:1024–1037.
43. Kjolby BF, Ostergaard L, Kiselev VG. Theoretical model of intravascular paramagnetic tracers effect on tissue relaxation. *Magn Reson Med* 2006;56:187–197.
44. Straka M, Schmiedeskamp H, Zaharchuk G, Andre JB, Olivot J-M, Fischbein NJ, Lansberg MG, Moseley ME, Albers GW, Bammer R. Spin-echo and gradient-echo PWI CBF vs. ASL CBF: an initial comparison. In: *Proceedings of the 19th Annual Meeting of the ISMRM*, Montreal, Canada; 2011. p 1972.
45. Schmiedeskamp H, Straka M, Jenuleson D, Zaharchuk G, Bammer R. T1-independent vessel size imaging with multi-gradient- and spin-echo EPI. In: *Proceedings of the Joint Annual Meeting of ISMRM/ESMRMB*, Stockholm, Sweden; 2010. p 1785.
46. Ostergaard L, Sorensen AG, Kwong KK, Weisskoff RM, Gyldensted C, Rosen BR. High resolution measurement of cerebral blood flow using intravascular tracer bolus passages. II. Experimental comparison and preliminary results. *Magn Reson Med* 1996;36:726–736.
47. Ostergaard L, Weisskoff RM, Chesler DA, Gyldensted C, Rosen BR. High resolution measurement of cerebral blood flow using intravascular tracer bolus passages. I. Mathematical approach and statistical analysis. *Magn Reson Med* 1996;36:715–725.
48. van Osch MJ, Vonken EJ, Viergever MA, van der Grond J, Bakker CJ. Measuring the arterial input function with gradient echo sequences. *Magn Reson Med* 2003;49:1067–1076.
49. Ellinger R, Kremser C, Schocke MF, Kolbitsch C, Griebel J, Felber SR, Aichner FT. The impact of peak saturation of the arterial input function on quantitative evaluation of dynamic susceptibility contrast-enhanced MR studies. *J Comput Assist Tomogr* 2000;24:942–948.
50. Jochimsen TH, Newbould RD, Skare ST, Clayton DB, Albers GW, Moseley ME, Bammer R. Identifying systematic errors in quantitative dynamic-susceptibility contrast perfusion imaging by high-resolution multi-echo parallel EPI. *NMR Biomed* 2007;20:429–438.
51. Bleeker EJ, van Buchem MA, van Osch MJ. Optimal location for arterial input function measurements near the middle cerebral artery in first-pass perfusion MRI. *J Cereb Blood Flow Metab* 2009;29:840–852.
52. Straka M, Schmiedeskamp H, Zaharchuk G, Andre JB, Olivot J-M, Fischbein NJ, Lansberg MG, Moseley ME, Albers GW, Bammer R. Consequences of multi-echo fits in perfusion MRI for the determination of MTT in presence of T1-effects. In: *Proceedings of the 19th Annual Meeting of the ISMRM*, Montreal, Canada; 2011. p 462.
53. Kiselev VG. Transverse relaxation effect of MRI contrast agents: a crucial issue for quantitative measurements of cerebral perfusion. *J Magn Reson Imaging* 2005;22:693–696.
54. Zaharchuk G, Straka M, Marks MP, Albers GW, Moseley ME, Bammer R. Combined arterial spin label and dynamic susceptibility contrast measurement of cerebral blood flow. *Magn Reson Med* 2010;63:1548–1556.
55. Christen T, Schmiedeskamp H, Straka M, Bammer R, Zaharchuk G. Rapid measurement of oxygen extraction fraction (OEF) maps using a combined multiple gradient and spin echo bolus contrast sequence. In: *Proceedings of the 19th Annual Meeting of ISMRM*, Montreal, Canada; 2011. p 2729.